A Hybrid Modulation Strategy Based on Tandem-Half-Bridge WPT Converter for Efficiency Optimization Within Wide Operation Range

Mingyang Li, *Graduate Student Member, IEEE*, Junjun Deng, *Member, IEEE*, Zhenyuan Zhang, *Graduate Student Member, IEEE*, and Zhenpo Wang, *Senior Member, IEEE*

***Abstract*—The efficiency of the wireless power transfer (WPT) system is highly dependent on the load resistance. To meet the demand of wide load variation, traditional methods employ dual-side control with multivariable to improve the efficiency for light loads. However, these methods often necessitate high-frequency signal synchronization and involve complex control. Therefore, a crucial challenge in WPT systems is to maintain high efficiency over a wide load range while using a simple control method. To address this research gap, a tandem-half-bridge (THB) WPT converter is proposed to improve the system efficiency and reduce the switching drain-source voltage. Based on the THB WPT converter, a hybrid modulation strategy is proposed, and only pulse frequency modulation or phase shift modulation is used in each operation mode. Additionally, a unified pulsewidth modulation generated method for three modes is given, which can be better applied in the digital controller. To validate the effectiveness of the proposed THB WPT converter under the hybrid modulation strategy, we construct a 1.8-kW experimental prototype. The experimental results demonstrate a peak efficiency of 95.26%. Furthermore, the efficiency under light load is up to 10.36% higher than the traditional full-bridge and half-bridge (FB&HB) converter under the mode switching strategy.**

***Index Terms*—Phase shift modulation (PSM), pulse frequency modulation (PFM), tandem-half-bridge (THB) topology, wide load range, wireless power transfer (WPT).**

I. Introduction

WIRELESS power transfer (WPT) technology [1], [2], [3] can use electromagnetic fields to deliver power to loads without contact, realizing electrical and mechanical isolation. This convenient charging method can change our traditional utilization patterns of energy in various applications, such as biomedical implants powering [4], [5], marine transports [6], and electric vehicles (EVs) [7], [8].

Manuscript received 9 August 2023; revised 26 October 2023 and 27 November 2023; accepted 15 December 2023. Date of publication 25 December 2023; date of current version 16 February 2024. This work was supported by the National Natural Science Foundation of China under Grant 52177207. Recommended for publication by Associate Editor J. Acero. *(Corresponding author: Junjun Deng.)*

The authors are with the Beijing Institute of Technology, Beijing 100081, China (e-mail: limingyang@bit.edu.cn; dengjunjun@bit.edu.cn; 3220210325@bit.edu.cn; wangzhenpo@bit.edu.cn).

Color versions of one or more figures in this article are available at https://doi.org/10.1109/TPEL.2023.3347003.

Digital Object Identifier 10.1109/TPEL.2023.3347003

Among these applications, wireless charging for EVs has gained popularity. To ensure high-efficiency charging throughout the process, the constant current-constant voltage charging regime has been widely adopted for EV charging [9], [10]. However, the equivalent load resistance of the EV battery pack can vary significantly, ranging from a few ohms to several hundred ohms, across the entire charge range [11]. Consequently, it is a great challenge to optimize system efficiency over a wide range of loads.

The two-stage WPT system with an additional dc–dc converter can solve this problem effectively, which can regulate the equivalent load of the system by adjusting the input voltage or output voltage of the WPT stage so that the system can still operate at the high-efficiency point when the battery load varies during the charging process [12], [13]. However, it is important to note that the inclusion of an additional dc/dc stage increases both the cost and control complexity of the system.

Alternatively, the single-stage WPT system without dc/dc stage has been widely investigated in EV charging applications since it does not need to incorporate an additional dc/dc stage, which can significantly improve the power density of the system as well as reduce the cost. However, without primary or secondary dc/dc, the WPT system also faces higher requirements under wide-range operation, and scholars have further optimized the performance of the single-stage WPT system for the wide-range operation with respect to the modulation strategy [14], [15], [16], [17], [18], [19], [20], [21], [22], mode switching [23], [24], [25], and power topology [26], [27].

The modulation strategies proposed for efficiency optimization over a wide range of operations are essentially an expansion of the control variables of the system. These strategies aim to decouple additional control variables to optimize system efficiency at light and medium loads while regulating the output voltage. They can be divided into two main types, one is uncontrolled rectification [14], [15], [16], the other is active rectification on the secondary side [17], [18], [19], [20], [21], [22]; both require signal synchronization techniques.

1) An uncontrolled rectifier bridge is used on the secondary side, which simplifies the system without the need for high-frequency (HF) signal synchronization. In [14] and

[15], variable frequency phase shift modulation (PSM) strategies are proposed for different compensation topologies, respectively. However, this method couples the frequency variable with the phase shift angle, which is not resolvable and can only be applied with the look-up table. Without using a frequency variable, Wang et al. [16] proposed a hybrid control strategy of PSM with the switch-controlled capacitor (SCC), which reduced the reactive current of the system by adjusting the value of the equivalent compensation capacitor, thus improving the system efficiency at light load. However, the inclusion of two additional switches increased the switching loss and system cost.

2) An active rectifier bridge is used on the secondary side so that two degrees of freedom can be expanded. Li et al. [18] proposed a dual-phase-shift (DPS) modulation strategy based on the dual-active-bridge (DAB) WPT converter, and the system efficiency can be improved due to the decrease of the maximum value of current stresses on both sides. Based on [18] and [20], a triple-phase-shift (TPS) modulation strategy by introducing the third phase shift angle, which suppresses reactive currents and realizes zero voltage switching (ZVS) to maintain high efficiency at the light load. However, these dual-side modulation strategies are based on DAB topology, which are hard to be applied in practice due to HF signal synchronization. Mai et al. [19] and Wu et al. [22] incorporated the auxiliary circuits and auxiliary windings to synchronize HF switching signals, respectively. Both of them can be calibrated to operate stably at the rated power point, but at half load and light load conditions, they may fail signal synchronization due to HF noise and hysteresis delay, and will not follow the efficient control trajectory. Moreover, one or more expensive HF current transducers are required in these methods.

To further optimize the efficiency over the wide operation range, the idea of reconfigurability between full-bridge and half-bridge operations has been presented in [23], [24], and [25]. These methods reduce the excitation voltage by switching the half-bridge mode at light load, thus decreasing the control redundancy of the system, and suppressing the reactive current at light load. However, these methods add mode switching on top of multivariable coupled control, which further increases the control complexity of the system. At the same time, there is a phenomenon of sudden change of variables during mode switching, which may cause control instability.

The above literature provides effective solutions to the problem of low efficiency over a wide operation range, but these multivariable control methods involve problems such as variable coupling and the inability to obtain an analytical solution. Moreover, single variable control strategies like single pulse frequency modulation (PFM) control and single-PSM control are simple, but they have a limited range of power regulation and excessive light-load reactive current, which are not suitable for wide-range applications. Therefore, to satisfy the system requirements under wide-range operation using simple topologies and control strategies, Zhu et al. [26] and Zhang et al. [27] proposed new power topologies with corresponding control strategies. Zhu et al. [26] proposed a dual half-bridge structure combined with a variable inductor, which can achieve high efficiency over a wide range with simple control methods, and it has a significant efficiency improvement compared to traditional single-phase-shift (SPS) control. Zhang et al. [27] proposed a simple single-switch inverter topology, which can maintain high overall efficiency even below half load. However, the single-switch structure makes the switching drain-source voltage much larger than the dc input voltage.

In addition, the EV WPT system needs to meet the charging demand of high-voltage and high-power batteries in different charging states, and the bus voltage after grid-side three-phase PFC rectification is generally above 700 V. In this case, for the single-stage WPT system, in addition to solving the problem of realizing high efficiency over a wide operation range with simple topology and practical control strategy, another challenge also remains on how to reduce the drain-source voltage of the switches without adopting the front-stage dc/dc.

In response, this article proposes a novel tandem-half-bridge (THB) WPT converter with a hybrid modulation strategy to solve the above-mentioned problems. The main contributions can be summarized as follows.

1) To get rid of dual-side control and auxiliary components, a novel WPT converter based on the THB topology is proposed for wide-range efficiency optimization. The proposed converter can reduce switching drain-source voltage at all loads and switching frequency at light loads, thus reducing the switching loss.
2) Based on the THB WPT converter, three operating modes are identified and analyzed for wide power range operation. These hybrid modes can equalize the voltage across the input capacitors, and can effectively avoid or suppress variable mutation at the switching boundaries, thus simplifying the control complexity and improving control stability.
3) According to the three operating modes, a hybrid modulation strategy is proposed to decrease switching loss and on-state loss at light load and medium load, which broadens the efficient working area of the system. In addition, only a single PFM or single PSM is used in each operation mode, so the power autoregulation can be realized by using a simple segmented PI control method, which can be better applied in practical applications.

The rest of this article is organized as follows. The proposed THB WPT converter and its operation principle are analyzed in Section II. Section III provides series-series (SS) WPT system characteristics analysis and mode configuration. In Section IV, the proposed control strategy is described, and the unified pulsewidth modulation (PWM)–generated method is given. In Section V, a prototype with 1.8 kW output power is presented to validate the proposed system, and the comparison of the proposed THB WPT converter with the reported literature is carried out. Finally, Section VI, concludes this article.

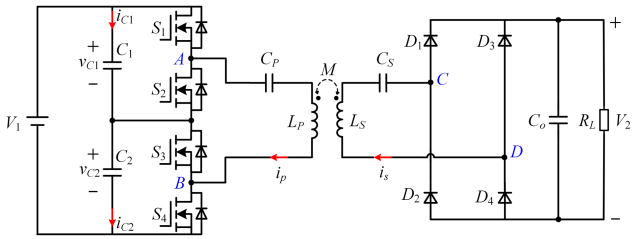

Fig. 1. Proposed THB WPT converter.

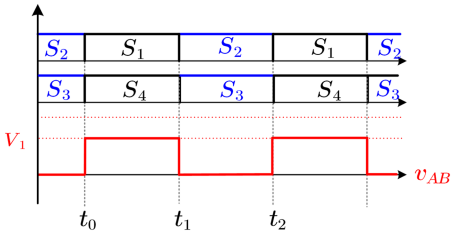

Fig. 2. Typical waveforms under 2-FIV mode.

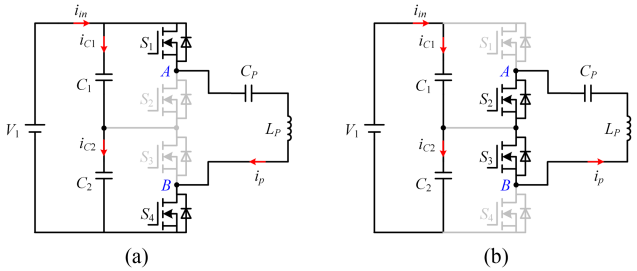

Fig. 3. Topological stages under 2-FIV mode. (a) State 1 [t_0–t_1] (b) State 2 [t_1–t_2].

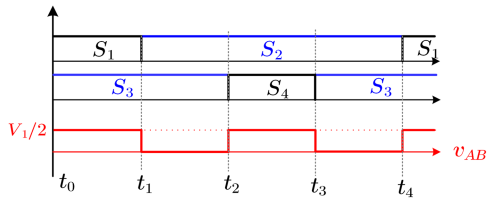

Fig. 4. Typical waveforms under 2-HIV mode.

II. Proposed Circuit Topology and Operation Principles

Fig. 1 shows the proposed THB WPT converter that is composed of two half-bridge circuits in series connection on the primary side, which includes four switching devices S_1 to S_4 and dc-link capacitors C_1 and C_2. The symmetric SS compensation network is employed in this article. In the resonant tanks, L_P and L_S are the self-inductances of the primary side coil and secondary side coil, respectively. M is the mutual inductance of the loosely coupled transformer. To minimize the reactive power, C_P and C_S are resonant capacitors adopted to compensate L_P and L_S. The input and output dc voltage are V_1 and V_2, respectively. v_{AB} and v_{CD} are the output voltages of the inverter and input voltage of the rectifier, respectively. f_r is defined as resonant frequency, which is set to be 85 kHz, according to the SAE J2954 standards for EVs [28].

Based on the THB circuit topology, the inverter has three operating modes by reconfiguring different modulation schemes, which corresponds to three power levels. The three operating modes are two-level-full-input-voltage (2-FIV) mode, two-level-half-input-voltage (2-HIV) mode, and three-level-phase-shift (3-PS) mode. To avoid overcurrent, the switches on the same half-bridge arms should be controlled for complementary conduction in either mode.

A. Two-Level-Full-Input-Voltage Mode

Figs. 2 and 3 show the typical waveforms and topological stages under the 2-FIV mode, respectively, which are applicable to high power levels. In this mode, S_1 and S_4 (S_2 and S_3) are turned ON and OFF simultaneously. When S_1 and S_4 are turned ON, the excitation voltage v_{AB} equals source voltage V_1, and when S_1 and S_4 are turned OFF, the excitation voltage v_{AB} is zero. The resonant current i_p does not flow through two dc-link capacitors, so C_1 and C_2 will share the source voltage V_1 equally.

Moreover, when the co-conduction time of S_1 and S_4 deviates from half of the switching period, it will cause uneven voltage division between C_1 and C_2, so the traditional PSM cannot be applied in this mode. In contrast, pulse frequency has no effect on the voltages of C_1 and C_2, so PFM can be used in this mode.

B. Two-Level-Half-Input-Voltage Mode

Fig. 4 shows the typical waveforms under the 2-HIV mode, which is applicable to low power levels. In this mode, turn-ON time of S_1 (S_4) occupies the 1/4th of the switching cycle, and the turn-ON time of S_2 (S_3) occupies the 3/4th of the switching cycle. Moreover, to satisfy the equalized voltage of C_1 and C_2, the co-conduction time of two switches on different bridge arms is fixed at 1/4th of the switching cycle. It can be seen from Fig. 4 that the switching frequency is half the frequency of the excitation voltage v_{AB}.

Fig. 5 illustrates four switching states under the 2-HIV mode. In State 1, S_1 and S_3 are turned ON, the excitation voltage v_{AB} is equal to the voltage across C_1. In State 2, S_2 and S_3 are turned ON, the excitation voltage v_{AB} is zero. In State 3, S_2 and S_4 are turned ON, the excitation voltage v_{AB} is equal to the voltage across C_2. In State 4, S_2 and S_3 are turned ON, the excitation voltage v_{AB} is zero. It should be noted that the charging and discharging processes of C_1 and C_2 are symmetrical in States 1 and 3, so the voltages across C_1 and C_2 can be considered as half of the source voltage V_1. Therefore, in this mode, v_{AB} is always half-voltage state and its frequency is twice the switching frequency. It can be observed from (1) that reducing switching frequency and the value of V_{DS} can reduce switching loss. Therefore, the switching loss can be significantly decreased compared with the traditional method.

$$P_{sw} = \frac{f_s V_{DS}}{1000 V_{DD}} (a_1 I_{DS}^2 - a_2 I_{DS} + a_3). \tag{1}$$

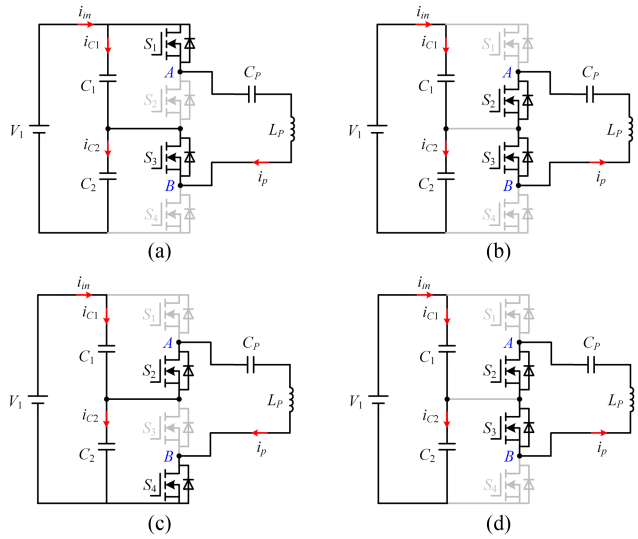

Fig. 5. Topological stages under 2-HIV mode. (a) State 1 [t_0–t_1]. (b) State 2 [t_1–t_2]. (c) State 3 [t_2–t_3]. (d) State 4 [t_3–t_4].

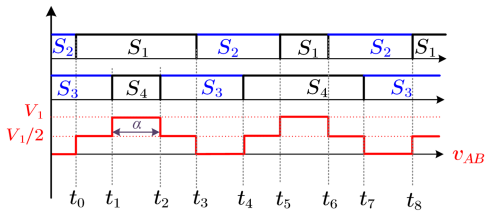

Fig. 6. Typical waveforms under 3-PS mode.

where V_{DD} is drain voltage under test conditions, *VDS* and *IDS* are the voltage and current stress when the switch is turn-OFF or turn-ON, respectively, and a_i is a fitting parameter for different switch models.

In addition, the conventional PSM is also unsuitable for this mode, as the charging and discharging processes of C_1 and C_2 are no longer symmetrical when the phase shifts, which leads to uneven voltage, so PFM is also used in this mode.

C. Three-Level-Phase-Shift Mode

The 2-FIV mode and 2-HIV mode both use PFM for high power and low power levels, however, it is still difficult to cover the medium power range with high efficiency due to the limitation of the narrow frequency regulation range for wireless charging system, so the 3-PS mode with double cycle modulation is proposed for medium power level, as shown in Fig. 6. In one switching cycle, all switches will turn ON and OFF twice. The pulse widths of S_2 and S_3 are set to $\pi/2$, and the pulse widths of S_1 and S_4 switch between α and π-α. Hence, the transfer power can be regulated by changing the value of α in this mode.

Fig. 7 illustrates four switching states under 3-PS mode. As shown in Fig. 7, in States 1 and States 3, S_1 and S_3 are turned ON, starting the charging/discharging process of C_1 and C_2. In States 5 and States 7, S_2 and S_4 are turned ON, and the charging/discharging process of C_1 and C_2 is also started at this time. To satisfy the equalized voltage of C_1 and C_2, the co-conduction time of two switches on different bridge arms is set at the same value so that the charging/discharging process of C_1 and C_2 is totally symmetrical during the whole switching cycle.

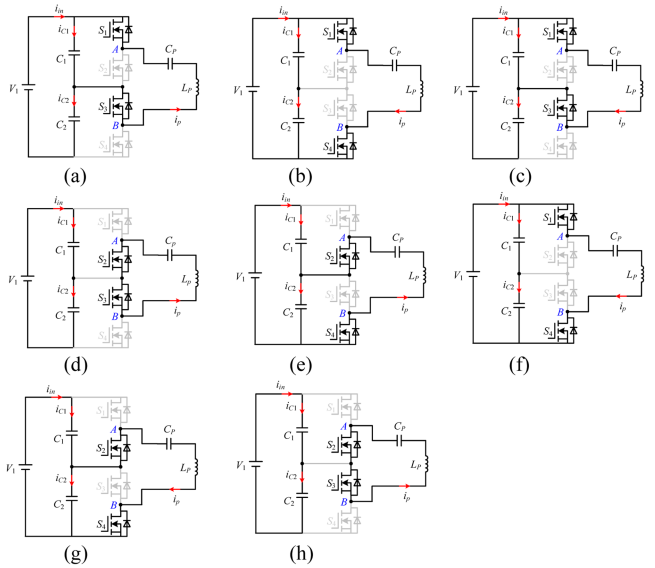

Fig. 7. Topological stages under 3-PS mode. (a) State 1 [t_0–t_1]. (b) State 2 [t_1–t_2]. (c) State 3 [t_2–t_3]. (d) State 4 [t_3–t_4]. (e) State 5 [t_4–t_5]. (f) State 6 [t_5–t_6]. (g) State 7 [t_6–t_7]. (h) State 8 [t_7–t_8].

III. System Characteristics Analysis and Resonant Tank Parameter Design

The previous section discussed the operation principles of the proposed THB WPT converter and topological stages in different modes. In this section, we will continue to analyze the system characteristics in conjunction with the compensation network, as well as the corresponding mode configurations and mode operation boundary delineation, and propose a parameter design method according to the system characteristics.

This section will introduce the basic modeling of SS WPT topology first. Then, based on SS topology modeling, the characteristics of the THB WPT system under different modes are analyzed. Accordingly, the mode-switching boundaries are delineated by calculating the power boundaries for each mode. Furthermore, the output power and input impedance angle in the 2-FIV mode are analyzed to obtain the resonant tank parameters.

A. SS Topology Modeling

Fig. 8 shows the ac equivalent circuit based on the fundamental harmonic model. The equivalent operating angular frequency of the inverter is represented by $\omega_{\mathrm{eq},s}$, which is equal to the switching angular frequency in 2-FIV mode, and twice the switching angular frequency in 2-HIV mode and 3-PS mode. For simplicity, the resonant angular frequency in primary and the resonant angular frequency in secondary are set to be equal to ω_r, which satisfies the following equation (ω_n is the normalized

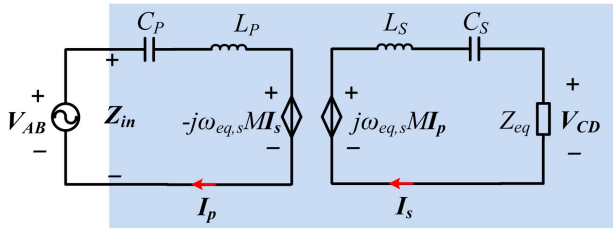

Fig. 8. AC equivalent circuit of SS compensated topology.

operating angular frequency that is defined as $\omega_{\mathrm{eq},s}/\omega_r$):

$$\omega_r = \frac{1}{\sqrt{L_P C_P}} = \frac{1}{\sqrt{L_S C_S}}. \tag{2}$$

For a diode rectifier, its equivalent resistance on the secondary side can be expressed as

$$Z_{\mathrm{eq}} = \frac{8R_L}{\pi^2}. \tag{3}$$

According to Kirchhoff's voltage law, the circuit model in Fig. 8 can be expressed at fundamental frequency as

$$\begin{cases} \dot{V_{AB}} - Z_P \dot{I}_p + j\omega_n\omega_r M \dot{I}_s = 0 \\ \dot{I}_s Z_{\mathrm{eq}} + Z_S \dot{I}_s - j\omega_n\omega_r M \dot{I}_p = 0 \end{cases}. \tag{4}$$

where Z_P is the primary resonant network impedance, which is $Z_P = j\omega_n\omega_r L_P + 1/(j\omega_n\omega_r C_P)$ and Z_S is the secondary resonant network impedance, which is $Z_S = j\omega_n\omega_r L_S + 1/(j\omega_n\omega_r C_S)$.

Based on the relationship of $\boldsymbol{I_s}$ and $\boldsymbol{I_p}$ in (4), the equivalent impedance reflected to the primary side $Z_{p,\mathrm{eq}}$ and the input impedance Z_{in} can be obtained as

$$Z_{\mathrm{in}} = Z_P + Z_{p,\mathrm{eq}} = Z_P + \frac{\omega_n^2\omega_r^2 M^2}{Z_S + Z_{\mathrm{eq}}}. \tag{5}$$

Then, the input impedance angle φ_{in} can be further acquired as (6) shown at the bottom of the next page. DC voltage gain G_v can be derived as (7) shown at the bottom of the next page by solving I_s in (4), where H_p is defined as V_{AB}/V_1, which varies in different modes.

B. Characteristics of the System Under Three Operating Modes

In this section, we will analyze the frequency characteristics of the 2-FIV and 2-HIV modes and the phase shift characteristic of the 3-PS mode. Accordingly, the effects of dc voltage gain, output power, and input impedance angle are discussed. In addition, the three modes are configured into the low-middle-high power range according to the mode characteristics so that the system can work efficiently in a wide power range.

1) Frequency Characteristic of 2-FIV Mode: In this mode, according to Fig. 2, the voltage scaling factor H_p satisfies (8).

$$H_p = \frac{V_{AB}}{V_1} = \frac{\sqrt{2}}{\pi}. \tag{8}$$

Therefore, based on (6) and (7), the dc voltage gain G_v and the input impedance angle φ_{in} versus ω_n in 2-FIV mode can be illustrated in Fig. 9. At the dc voltage gain of 0.375, two alternative regions can achieve ZVS, ZVS1 region and ZVS2 region, as shown in Fig. 9. However, the input impedance angle is large in the ZVS2 region, which makes the reactive current in the resonant tank also large and affects the system efficiency, so $\omega_n < 1$ should be controlled in this mode to make the system work in the ZVS1 region. In addition, as the load R_L increases, the system will be unable to work in the ZVS1 region, so this mode is suitable for high power levels and has a minimum operating power boundary.

2) Frequency Characteristic of 2-HIV Mode: In this mode, according to Fig. 4, the voltage scaling factor H_p satisfies

$$H_p = \frac{V_{AB}}{V_1} = \frac{\sqrt{2}}{2\pi}. \tag{9}$$

Therefore, based on (7) and (8), the dc voltage gain G_v and the input impedance angle φ_{in} versus ω_n in 2-HIV mode can be illustrated in Fig. 10. At a dc voltage gain of 0.375, there is only one region that can achieve ZVS, as shown in Fig. 10. As the load R_L decreases, the system will not be able to work in the ZVS region, so this mode is suitable for low power level and has a maximum operating power boundary.

3) Phase Shift Characteristic of 3-PS Mode: In this mode, the normalized operating angular frequency ω_n is set as 1, hence the following equation is established:

$$\omega_{\mathrm{eq},s} = \omega_r = \frac{1}{\sqrt{L_P C_P}} = \frac{1}{\sqrt{L_S C_S}}. \tag{10}$$

Moreover, it can be seen from Fig. 6 that the equivalent duty cycle of the v_{AB} is α by 2π, so the fundamental component for the output voltage of the primary inverter can be derived as follows based on the Fourier series expansion:

$$\dot{V_{AB}} = \frac{\sqrt{2}V_1}{\pi} \cdot \sin\left(\frac{\alpha}{2}\right) \cdot \angle 0. \tag{11}$$

According to (4) and (10), Z_P and Z_S are zero in this mode, so the resonant current $\boldsymbol{I_s}$ and $\boldsymbol{I_p}$ can be simplified as

$$\dot{I}_s = -\frac{\dot{V_{AB}}}{j\omega_r M} \quad \dot{I}_p = \frac{\dot{V_{AB}} Z_{\mathrm{eq}}}{\omega_r^2 M^2}. \tag{12}$$

Then, the output power can be calculated as (13) under the premise of ignoring the system loss. Therefore, in the 3-PS mode, the output power can be adjusted by changing the value of α with the input and output voltages determined as

$$P_o = \frac{4V_1^2 G_v}{\pi^2\omega_r M} \sin\left(\frac{\alpha}{2}\right). \tag{13}$$

C. Mode Switching Boundary

As shown in Fig. 9, when the system works in the ZVS1 region, the increase in angular frequency will make the output power decrease, so the minimum operating power boundary P_{bd2} for this mode can be calculated when $\omega_n = 1$, which is expressed as

$$P_{bd2} = \frac{4V_1^2 G_v}{\pi^2\omega_r M}. \tag{14}$$

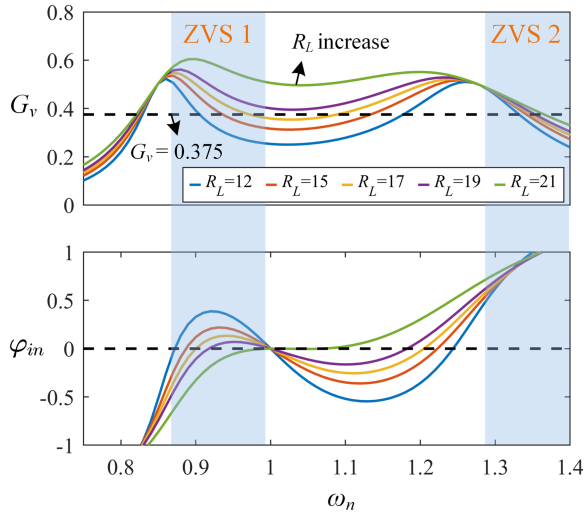

Fig. 9. DC voltage gain G_v and the input impedance angle $\varphi_{\rm in}$ versus ω_n in 2-FIV mode.

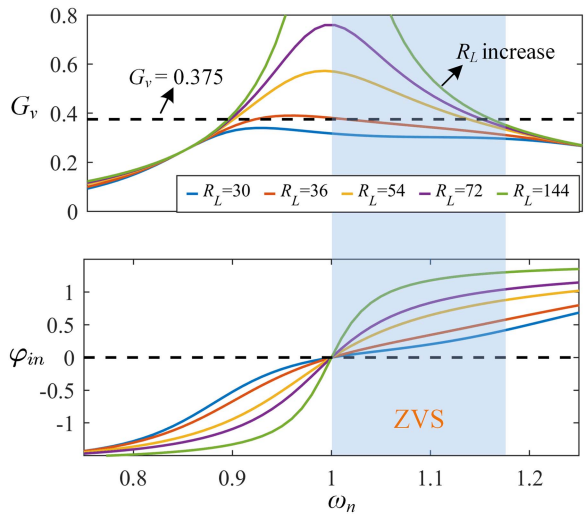

Fig. 10. DC voltage gain G_v and the input impedance angle $\varphi_{\rm in}$ versus ω_n in 2-HIV mode.

Similarly, as shown in Fig. 10, when the system works in the ZVS region, the decrease in angular frequency will cause an increase in the output power, so the maximum operating power boundary $P_{\rm bd1}$ for this mode can be calculated when $\omega_n = 1$,

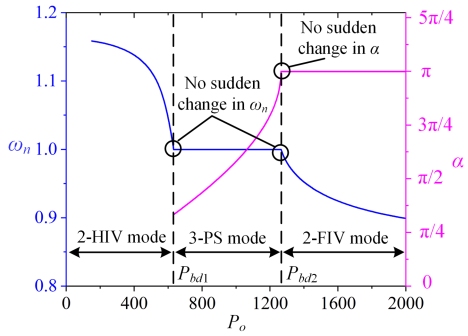

Fig. 11. Control trajectories of variables ω_n and α in each mode and mode switching boundary.

which is expressed as

$$P_{bd1} = \frac{2V_1^2 G_v}{\pi^2 \omega_r M}. \tag{15}$$

Fig. 11 shows the control trajectory of variables ω_n and α in each mode and corresponding mode switching boundaries. In the 2-HIV and 2-FIV modes, the output power is adjusted by changing the normalized operating angular frequency ω_n. However, in the 3-PS mode, the output power is adjusted by changing the phase shift angle α, and the equivalent operating angular frequency of the system is always kept at the resonant angular frequency in this mode. The power boundaries of the mode switching are $P_{\rm bd1}$ and $P_{\rm bd2}$, respectively. The proposed hybrid modulation strategy based on control trajectories in Fig. 11 can significantly decrease switching loss and ON-state loss at light load and medium load according to loss breakdown analysis, which broadens the working area of the system.

Moreover, it can be seen from Fig. 11 that the hybrid working modes can effectively avoid or suppress variable mutation at the switching boundaries, thus simplifying the control complexity and improving control stability.

D. Parameter Design

The symmetric SS compensation network is employed in this article, so $L_P = L_S$ holds in the following analysis, and here we only describe the criterion for selecting the primary parameters L_P and C_P. In Section III-B, it is mentioned that to expand the efficient working range of the system, the rated output power point of the system is not designed in the 3-PS mode, but in the 2-FIV mode under the PFM operation, so the selection of L_P should first satisfy the requirement of output rated power at the specific dc voltage gain G_v, as shown in (7).

$$\varphi_{\rm in} = \arctan\left[\frac{\mathrm{Im}[Z_{\rm in}]}{\mathrm{Re}[Z_{\rm in}]}\right] = \arctan\left[-\frac{(-\pi^4\omega_r^2 L_S^2 L_P(\omega_n+1)^2(\omega_n-1)^2 + \pi^4\omega_r^2\omega_n^4 M^2 L_S - 64\omega_n^2 R_L^2 L_P)(\omega_n+1)(\omega_n-1)}{8\pi^2\omega_r\omega_n^5 M^2 R_L}\right] \tag{6}$$

$$G_v = \frac{V_2}{V_1} = \frac{\pi H_p I_s Z_{\rm eq}}{2\sqrt{2}V_{AB}} = \frac{2\sqrt{2}H_P\pi\omega_n^3 M R_L}{\sqrt{\pi^4\omega_r^2(-L_P L_S(\omega_n+1)^2(\omega_n-1)^2 + \omega_n^4 M^2)^2 + 64\omega_n^2 L_P^2 R_L^2(\omega_n+1)^2(\omega_n-1)^2}} \tag{7}$$

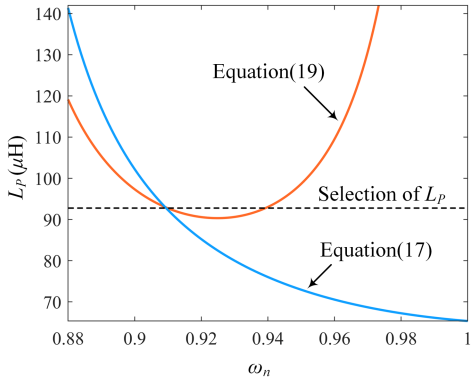

Fig. 12. Selection of parameter L_P in operation principles.

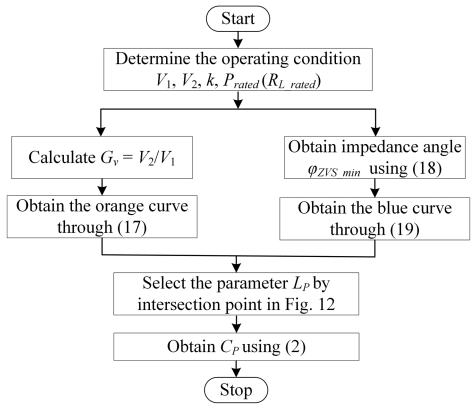

Fig. 13. Flowchart of the criterion for selecting the parameters L_P and C_P.

The coupling coefficient k of the WPT system is defined as

$$M = k\sqrt{L_P L_S}. \tag{16}$$

Based on the assumption of $L_P = L_S$ and (16), (7) can be transformed as (17). It can be seen from that when the operating conditions of the system are determined, the one relationship between L_P and the ω_n can be described as the blue curve in Fig. 12.

$$L_P = \frac{4\omega_n R_{L\_\text{rated}}\sqrt{\omega_n^4 k^2 - 4G_v^2(\omega_n+1)^2(\omega_n-1)^2}}{\pi^2 G_v \omega_r(-(\omega_n+1)^2(\omega_n-1)^2 + \omega_n^4 k^2)}. \tag{17}$$

On the other hand, the selection of the parameter L_P also affects the input impedance angle at the rated power, and the minimal input impedance angle to realize soft switching is defined as $\varphi_{\text{ZVS\_min}}$. To discharge the junction capacitors of MOSFET within the dead time for ZVS operation, the input impendence angle φ_{ZVS} should satisfy (18), where C_{oss} is the junction capacitance of MOSFETs, t_d is the dead time, and a 10% margin is also taken in case the parameters drift occurs [15]. Due to the symmetry of the driver pulses and the resonant current in 2-FIV mode, as long as S_1 can achieve ZVS, the ZVS operation of all switches can be achieved. Moreover, the minimum quantity of electric charge of the corresponding Q_x for achieving ZVS can be represented as Q_{ZVSxmin}, which corresponds to $\varphi_{\text{ZVS\_min}}$.

$$\begin{aligned} Q_{\text{ZVS1}} &= 90\% \left| \int_{\frac{\varphi_{\text{ZVS}}}{2\pi f_{\text{eq},s}}}^{\frac{\varphi_{\text{ZVS}}}{2\pi f_{\text{eq},s}}+t_d} i_p dt \right| \geq \int_0^{V_1/2} 2C_{oss1} dv \\ &= Q_{\text{ZVS1 min}}. \end{aligned} \tag{18}$$

When $L_P = L_S$ holds, (6) can be simplified as (19) shown at the bottom of this page. Hence, based on $\varphi_{\text{ZVS\_min}}$ and (19), the other relationship between L_P and the ω_n can be described as the orange curve in Fig. 12. Therefore, L_P can be selected according to the intersection point of the two curves in Fig. 12.

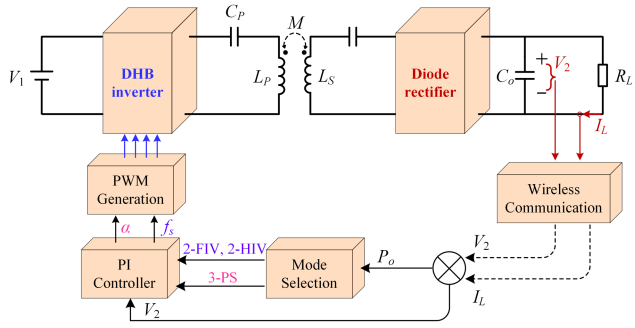

Fig. 14. Proposed control diagram for the WPT system.

L_P and C_P satisfy the relationship in (2) at the resonant frequency, so after L_P is determined, C_P can be obtained from (2). In summary, the criterion for selecting the parameters L_P and C_P in operation principles is shown in Fig. 13.

IV. Proposed Control Strategy

A. Proposed Control Strategy

The block diagram of the proposed control strategy is depicted in Fig. 14. It mainly consists of a mode selection module and a PI controller. V_2 and I_L will be measured by the dc voltage sensor and dc current sensor, respectively, and sent to the primary side via a wireless communication module. Then, the output power P_o can be calculated and the operation mode will be selected based on (14) and (15). Meanwhile, V_2 will be sent to the PI controller and then the PI controller can give the values of α and f_s, respectively, according to the selected operating mode and the reference voltage. It should be noted that in the 2-HIV mode and 2-FIV mode, only f_s is regulated, and in the 3-PS mode only α is regulated.

$$\varphi_{\text{ZVS\_min}} = \arctan\left[-\frac{(-\pi^4\omega_r^2 L_P^2(\omega_n^2-1)^2 + \pi^4\omega_r^2\omega_n^4 k^2 L_P^2 - 64\omega_n^2 R_{L\_\text{rated}}^2)(\omega_n^2-1)}{8\pi^2\omega_r\omega_n^5 k^2 L_P R_{L\_\text{rated}}}\right]. \tag{19}$$

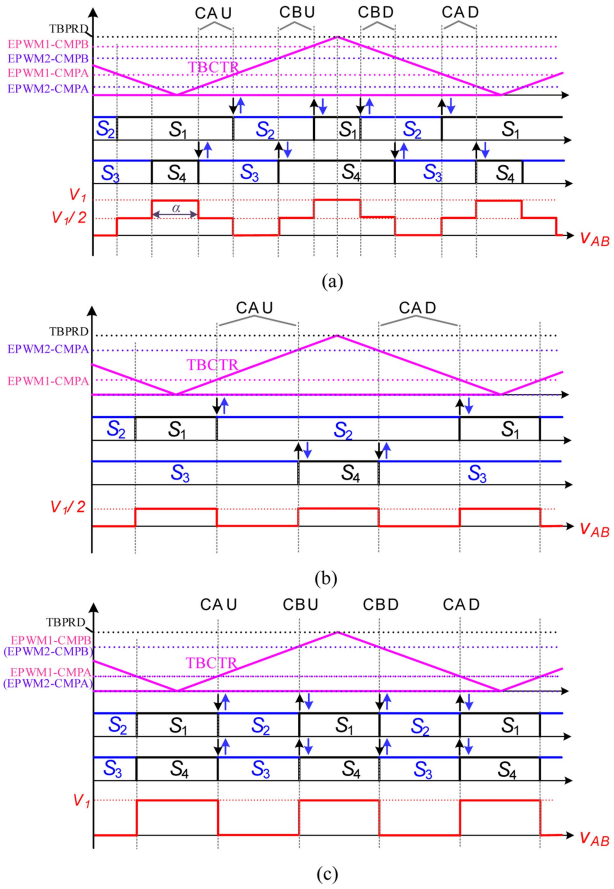

Fig. 15. Unified PWM generated method in three operation modes. (a) In the 3-PS mode. (b) In the 2-HIV mode. (c) In the 2-FIV mode.

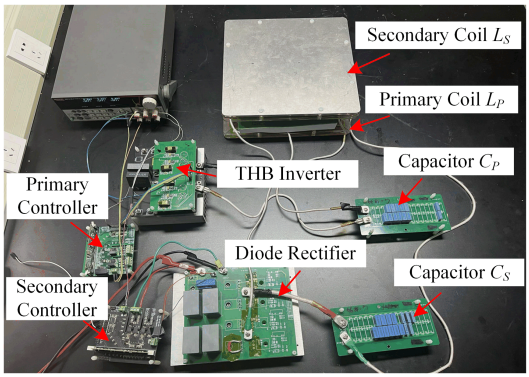

Fig. 16. Setup of the experimental prototype.

B. Unified PWM Generated Method

Fig. 15 shows the proposed unified PWM-generated method in three operation modes. TI DSP F28335 is used as the digital controller. Its enhanced PWM module is used to generate the PWM signals for driving the switches, and TBPRD is defined as the time-based period. In the traditional method, time-based counter TBCTR is configured with up-count mode or down-count mode. However, double-cycle modulation is utilized to equalize the voltage across input capacitors in the proposed control strategy, so large amounts of calculation and pulse loss may occur under the traditional PWM-generated method. Therefore, the up-down-count mode is used in the proposed PWM-generated method to solve the above-mentioned problems, which simplifies the control complexity and improves control stability. The operation mode can be selected by configuring two counter-compare values, CMPA and CMPB.

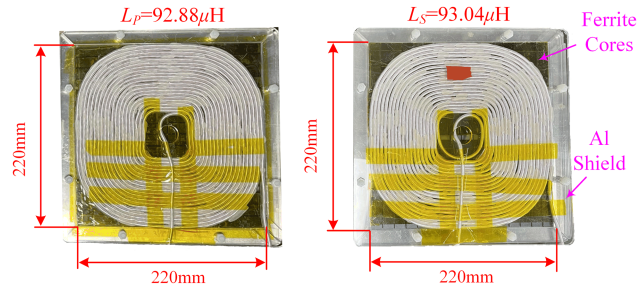

Fig. 17. Prototype of the magnetic coupler built in the laboratory.

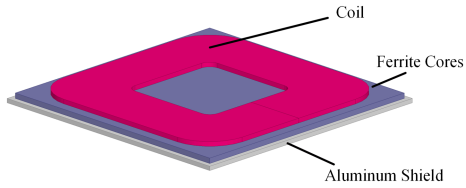

Fig. 18. 3-D model of magnetic coupler shielding structure.

For 3-PS mode, the counter-compare values of EPWM1 and EPWM2 are calculated as

$$\begin{cases} \text{EPWM1}-\text{CMPA} = (\frac{1}{2} - \frac{\alpha}{4\pi}) \cdot \text{TBPRD} \\ \text{EPWM1}-\text{CMPB} = (1 - \frac{\alpha}{4\pi}) \cdot \text{TBPRD} \\ \text{EPWM2}-\text{CMP}A = \frac{\alpha}{4\pi} \cdot \text{TBPRD} \\ \text{EPWM2}-\text{CMP}B = (\frac{1}{2} + \frac{\alpha}{4\pi}) \cdot \text{TBPRD} \end{cases}. \tag{20}$$

For 2-HIV mode, the counter-compare values of EPWM1 and EPWM2 are calculated as

$$\begin{cases} \text{EPWM1}-\text{CMPA} = \frac{1}{4} \cdot \text{TBPRD} \\ \text{EPWM2}-\text{CMPA} = \frac{3}{4} \cdot \text{TBPRD} \end{cases}. \tag{21}$$

For 2-FIV mode, the counter-compare values of EPWM1 and EPWM2 are calculated as

$$\begin{cases} \text{EPWM1}-\text{CMPA} = \text{EPWM2}-\text{CMPA} = \frac{1}{4} \cdot \text{TBPRD} \\ \text{EPWM1}-\text{CMPB} = \text{EPWM2}-\text{CMPB} = \frac{3}{4} \cdot \text{TBPRD} \end{cases}. \tag{22}$$

In addition, there are four events in the up-down-count mode: counter equals CMPA on up-count (CAU), counter equals CMPB on up-count (CBU), counter equals CMPB on down-count (CBD), and counter equals CMPA on down-count (CAD). When these four events are triggered, two actions of set-high and clear-low for drive waveforms can be executed, which are marked with upward and downward arrows, respectively, as shown in Fig. 15.

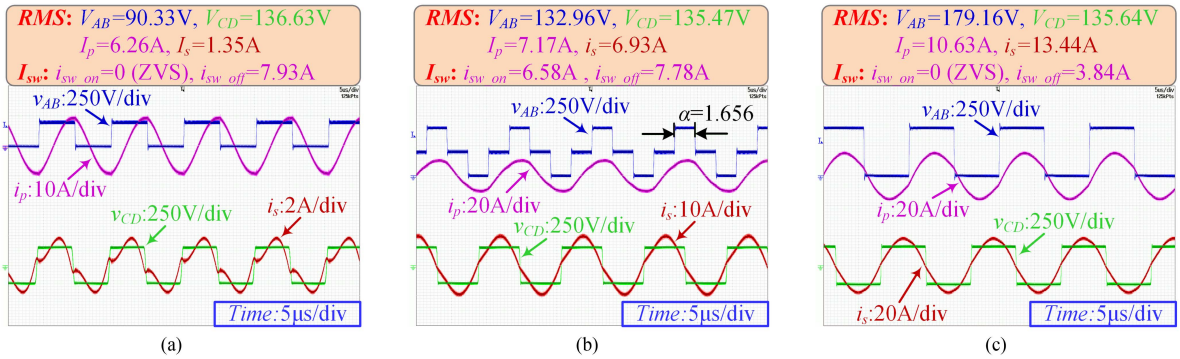

Fig. 19. Steady-state waveforms of THB WPT converter under the proposed hybrid modulation strategy. (a) $P_o = 150$ W in 2-HIV mode. (b) $P_o = 900$ W in 3-PS mode. (c) $P_o = 1800$ W in 2-FIV mode.

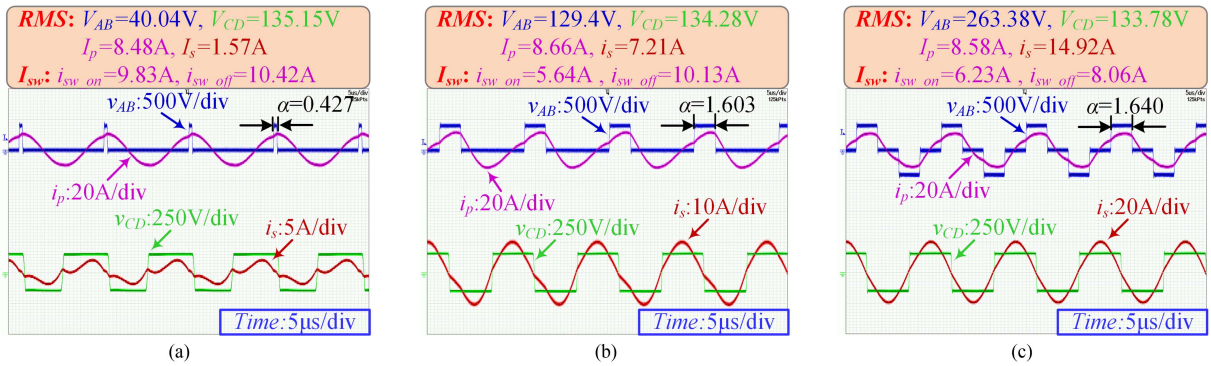

Fig. 20. Steady-state waveforms of TFHB WPT converter under the SPS modulation strategy. (a) $P_o = 150$ W at HB mode. (b) $P_o = 900$ W in HB mode. (c) $P_o = 1800$ W in FB mode.

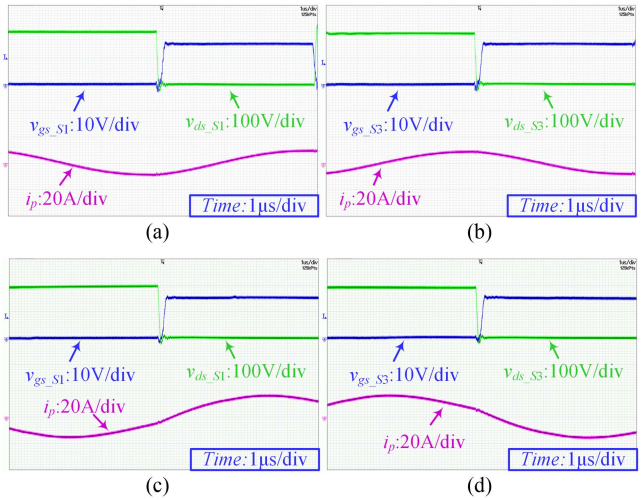

Fig. 21. Soft-switching waveforms for S_1 and S_3. (a) S_1 at $P_o = 150$ W. (b) S_3 at $P_o = 150$ W. (c) S_1 at $P_o = 1800$ W. (d) S_3 at $P_o = 1800$ W.

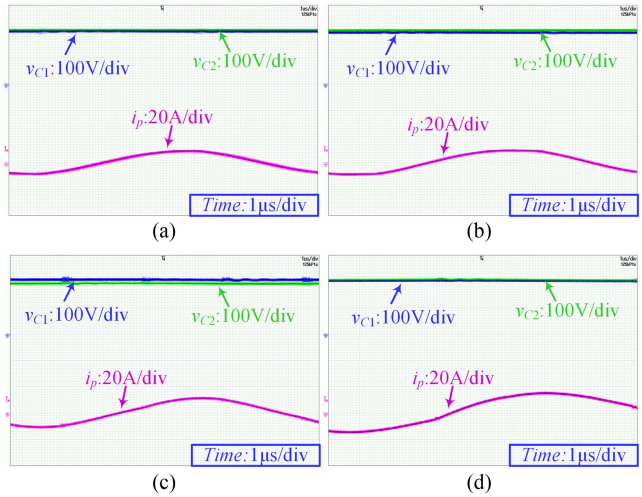

Fig. 22. Equalized voltage waveforms of capacitors C_1 and C_2. (a) $P_o = 150$ W. (b) $P_o = 300$ W. (c) $P_o = 900$ W. (d) $P_o = 1800$ W.

V. Experimental Verification

A. Hardware Prototype

A 1.8-kW prototype is designed to verify the rationality of the proposed WPT converter and the correctness of the theoretical analysis above. The setup of the experimental prototype is shown in Fig. 16. The circuit parameters of the experimental prototype are summarized in Table I. TMS320F28335DSP is implemented as the digital controller, and the power circuits are covered by the driver boards. Because the structure of THB allows for lower blocking voltage of MOSFETs, four silicon carbide power MOSFETs (C3M0045065D, 650 V, 49 A) are selected as S_1–S_4

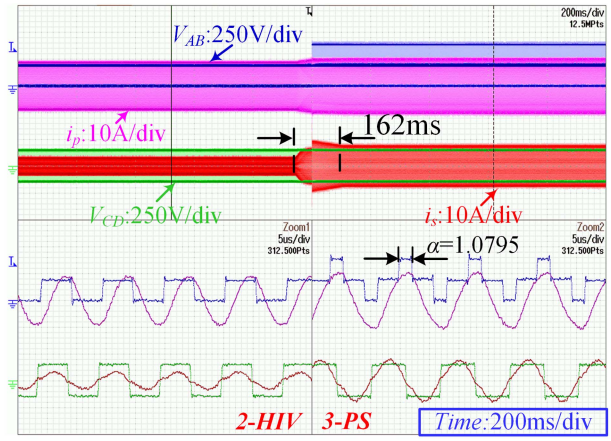

(a)

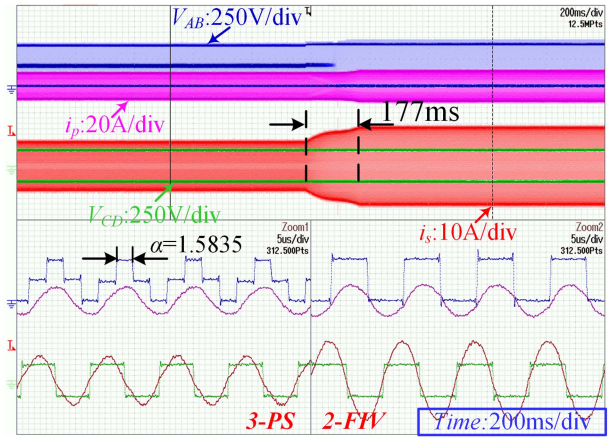

(b)

Fig. 23. Mode transient results for a load step change. (a) 400–750 W, 2-HIV mode to 3-PS mode. (b) 900–1500 W, 3-PS mode to 2-FIV mode.

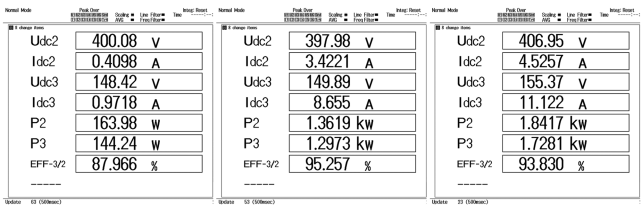

(a) (b) (c)

Fig. 24. Capture of power analyzer when delivering different power. (a) P_o = 150 W. (b) P_o = 1300 W. (c) P_o = 1800 W.

TABLE I
CIRCUIT PARAMETERS OF PROTOTYPE

Parameters	Value
Primary coil inductance, L_P	92.88 μH
Secondary coil inductance L_S	93.04 μH
Mutual inductance, M	35.92 μH
Primary series compensation capacitance, C_P	38.12 nF
Secondary series compensation capacitance, C_S	37.96 nF
Primary side resistance, $R_{LP}+R_{CP}$	218.56 mΩ
Primary side resistance, $R_{LS}+R_{CS}$	209.34 mΩ
Input voltage (V_1)	400 V
Output voltage (V_2)	150 V
Rated power (P_{rated})	1.8 kW
Resonant frequency (f_r)	85 kHz

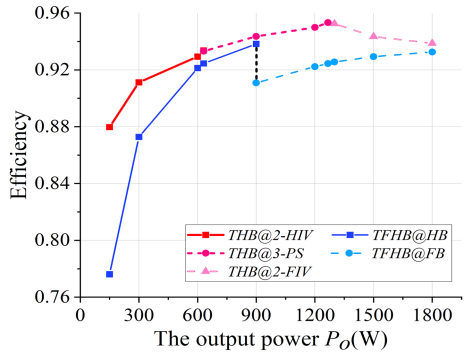

Fig. 25. Conversion efficiency of the THB converter and the TFHB converter.

for the THB inverter, which have low ON-resistance of 45 mΩ. Four Schottky diodes (C5D50065D, 650 V, 50 A) are used for the secondary rectifier.

The coil structure used in this article is a rectangular structure, which is built in the laboratory with parameters $L_P = 92.88\ \mu$H, $L_S = 93.04\ \mu$H, and physical dimensions of 220 mm $\times$ 220 mm, as shown in Fig. 17. To show the magnetic shielding structure more clearly, the 3-D model of magnetic coupler shielding structure from Maxwell is given in Fig. 18, where the first layer is the coil, the second layer is ferrite cores and the third layer is an aluminum shield.

B. Experimental Results

The steady-state waveforms of the THB converter under the proposed hybrid modulation strategy and the traditional full-bridge and half-bridge (FB&HB) (TFHB) converter under the SPS modulation strategy are shown in Figs. 19 and 20, respectively. The results show that the converter can operate stably over the full load range, validating the proposed control strategy. Moreover, Fig. 20 shows that, for the TFHB converter, the resonant current in the primary remains high at light load even when switching to HB mode, which increases both conduction and switching losses. In contrast, the maximum potential of PFM and PSM can be exploited by configuring the modes in each power range of the THB converter, which suppresses the resonant current. It can be drawn from Figs. 19 and 20 that at a light load of 150 W, the primary resonant current of the TFHB converter is 35.5% higher than that of the proposed THB converter, and the primary reactive current of the TFHB converter is 21.5% higher than that of the proposed THB converter.

Fig. 21 shows the specific soft switching waveforms under different loads, where v_{gs} is the driver signal and v_{ds} is the drain-source voltage. Due to the symmetry between the upper switch and the bottom switch in a half-bridge, only the soft switching waveforms of the upper switches are illustrated. Fig. 21(a) and (b) illustrates the ZVS occurrence of switches S_1 and S_3 at the light load under the 2-HIV mode, and Fig. 21(c) and (d) illustrates the ZVS occurrence of switches S_1 and S_3 at the full load under the 2-FIV mode. As seen, before v_{gs} changes from zero to positive, v_{ds} already goes to zero, so ZVS of S_1 and S_3 can be obtained in these two modes.

TABLE II
COMPARATIVE ANALYSIS OF THE PROPOSED THB CONVERTER WITH REPORTED LITERATURE

Reference	Switching drain-source voltage	Modulation scheme	Requirement of dual-side control	Auxiliary components	Control complexity	Testing output power range	Efficiency over the full range
[12]	V_{bus}	DPS	YES	Extra dc/dc	High	40%–100%	~85%–86%
[17]	V_{bus}	DPS	YES	Nil	Medium	20%–100%	~77%–94%
[18]	V_{bus}	DPS	YES	Nil	Medium	10%–100%	~77%–93%
[19]	V_{bus}	TPS	YES	Additional Coil	High	37.5%–100%	~91%–92%
[20]	V_{bus}	TPS	YES	Nil	Medium	20%–100%	~90%–94.8%
[16]	V_{bus}	SPS+SCC	NO	Extra SCC	High	20%–100%	~81%–94.7%
[29]	V_{bus}	SPS+DSCC	NO	Extra SCC	High	20%–100%	~88%–95.6%
[30]	V_{bus}	PDM	NO	Nil	High	25%–75%	89.8%–93.3%
[26]	V_{bus}	VIs modulation	NO	Variable Inductors	Medium	16.7%–100%	88%–92.4%
[27]	$max\sim= 4V_{bus}$	Duty cycle modulation	NO	Nil	High	25%–100%	86%–92.5%
This article	$V_{bus}/2$	Hybrid modulation	NO	Nil	Low	8.3%–100%	88%–95.3%

Fig. 22 illustrates the equalized voltage waveforms of capacitors C_1 and C_2. According to the topological stages analysis in Section II, when S_1 and S_3 are both turned ON, or S_2 and S_4 are both turned ON, the resonant current i_p will be involved in the charging and discharging process of capacitors C_1 and C_2. The proposed hybrid PWM method makes the capacitors C_1 and C_2 equal in charging and discharging voltages in one cycle, thus achieving voltage equalization of C_1 and C_2.

It can be seen from Fig. 22 that the voltage across C_1 and C_2 are both half of the input dc voltage from light load to full load, which is in accordance with the operating modes analysis in Section II. Moreover, the achievement of an equalized voltage of capacitors lowers the drain-source voltage of switches, which allows the MOSFETs with lower drain-source voltage to be selected.

With the intention to show the dynamic performance between the different operating modes of the experiment prototype, the dynamic waveform, when the output power is switched from 400 to 750 W is shown in Fig. 23(a). The dynamic waveform, when output power is switched from 900 to 1500 W is shown in Fig. 23(b). As seen, the output voltage of the rectifier V_{CD} can remain constant when the load changes. In addition, Fig. 23 indicates that the control is a seamless closed-loop control.

Figs. 24 and 25 illustrate the measured conversion efficiency of the THB converter under the proposed hybrid modulation strategy and the TFHB converter under the SPS mode switching modulation strategy, which is measured by power analyzer WT1800 supported by YOKOGAWA. The results show that the efficiency of the proposed THB WPT converter is consistently above 87.97% over the 8.3%–100% load range and the measured peak efficiency is achieved at about 95.26%. Meanwhile, it also can be seen that the efficiency of the proposed THB converter under the hybrid modulation strategy has significantly improved compared to the TFHB converter under the SPS modulation strategy, especially under the light load and half load conditions. In addition, it can be observed from Fig. 25 that the efficiency can be increased up to 10.36% at $P_o = 150$ W, 3.84% at $P_o = 300$ W, and 2.76% at $P_o = 1200$ W, which is a significant improvement.

The power loss of each component in the WPT system is shown in Fig. 26, which depicts various losses of the proposed THB converter and TFHB converter at different power levels. It can be seen from Fig. 26 that, at light load and medium load, the switching loss, conduction loss, and copper loss of the proposed THB converter can be reduced significantly compared with the TFHB converter. Moreover, at rated power, the switching loss can also be greatly reduced due to ZVS realization. The core loss is nearly similar under both converters at all power levels, but it accounts for the smallest proportion of the total efficiency loss.

C. Comparison

Table II shows the comparative analysis of the proposed THB converter with previously reported literature, with the goal of optimizing efficiency within a wide operation range. It can be seen from Table II that the proposed THB converter has lower switching blocking voltage for the same input voltage, which means MOSFETS with lower drain-source voltage can be selected, making it more cost-effective. Moreover, lower switching blocking voltage also means lower switching loss according to (1).

Compared with the first five papers with dual-side control, the proposed THB converter eliminates the need for active switches and signal synchronization on the receiver side, thereby reducing the overall complexity and system cost.

Compared with the last five papers with single-side control, the proposed THB converter can achieve high efficiency without the auxiliary components, whereas those presented in [27] and [30] also do not need the auxiliary components, they come at the cost of high control complexity and high current fluctuation. In addition, the proposed hybrid modulation strategy uses only a single PSM and single PFM control in each working mode, which avoids problems such as variable coupling and the inability to obtain an analytical solution, resulting in a low control complexity.

Moreover, for the key performance of efficiency over a wide operating range, the proposed system can achieve 91.6% of overall efficiency in the power range of 8.3%–100% and 88% efficiency even at 8.3% load, which is very favorable compared to both dual-side control system and single-side control system.

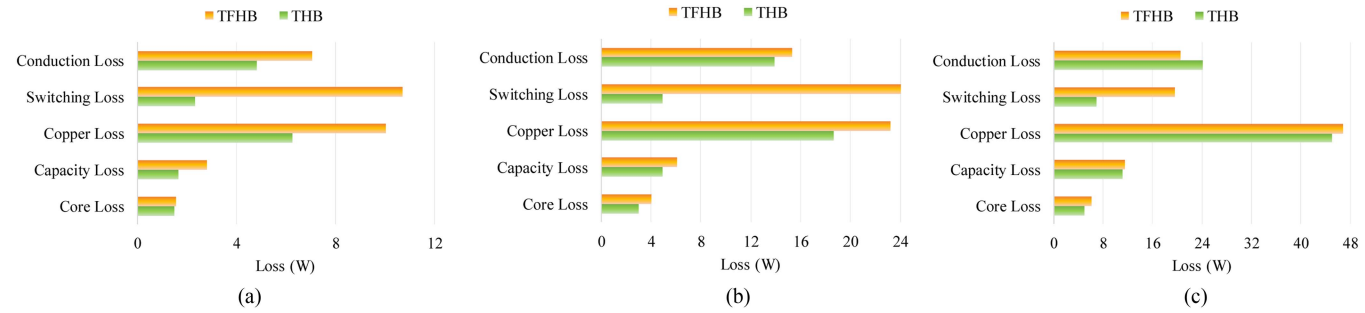

Fig. 26. Loss breakdown of proposed THB converter and TFHB converter at different power levels. (a) $P_o = 150$ W. (b) $P_o = 1200$ W. (c) $P_o = 1800$ W.

VI. Conclusion

In this article, the THB WPT converter is proposed to improve the system efficiency over the full operation range while simultaneously lowering the switching drain-source voltage. Then, three operating modes of the THB converter which can equalize the capacitor voltage are selected and analyzed. Accordingly, a hybrid modulation is proposed based on the frequency and phase-shift characteristics of the three modes, with the high-efficiency potential of PFM and PSM maximized in each control area. Moreover, a unified PWM-generated method is given to avoid inconsistent interval frequencies and loss of pulses during mode switching. The proposed THB converter with the hybrid modulation strategy is validated by comparison experiments with the traditional TFHB converter under the SPS mode switching modulation strategy. The results show that at $P_o = 150$ W (8.3% rated power), the efficiency of 87.97% can be achieved with a 10.36% increase, and at P_o=1200 W (66% rated power), the efficiency of 94.99% can be achieved with a 2.76% increase. Various load conditions have been applied to verify the performance of the proposed system.

Based on the topology and modulation strategy proposed in this article, to further improve the efficiency of the system at light load, active-rectifier technology with a multivariable phase-shift control strategy can be used. However, such light-load efficiency improvement also comes at the cost of control complexity and system cost, which should be considered in a holistic way.

References

[1] Z. Zhang, H. Pang, A. Georgiadis, and C. Cecati, "Wireless power transfer—An overview," *IEEE Trans. Ind. Electron.*, vol. 66, no. 2, pp. 1044–1058, Feb. 2019.

[2] S. Li, S. Lu, and C. C. Mi, "Revolution of electric vehicle charging technologies accelerated by wide bandgap devices," *Proc. IEEE*, vol. 109, no. 6, pp. 985–1003, Jun. 2021.

[3] N. Fu, J. Deng, Z. Wang, and D. Chen, "An *LCC–LCC* compensated WPT system with switch-controlled capacitor for improving efficiency at wide output voltages," *IEEE Trans. Power Electron.*, vol. 38, no. 7, pp. 9183–9194, Jul. 2023.

[4] M. R. Basar, M. Y. Ahmad, J. Cho, and F. Ibrahim, "An improved wearable resonant wireless power transfer system for biomedical capsule endoscope," *IEEE Trans. Ind. Electron.*, vol. 65, no. 10, pp. 7772–7781, Oct. 2018.

[5] S. Roy, A. N. M. W. Azad, S. Baidya, M. K. Alam, and F. Khan, "Powering solutions for biomedical sensors and implants inside the human body: A comprehensive review on energy harvesting units, energy storage, and wireless power transfer techniques," *IEEE Trans. Power Electron.*, vol. 37, no. 10, pp. 12237–12263, Oct. 2022.

[6] Z. Bie, J. Zhang, K. Song, D. Wang, and C. Zhu, "A free-rotation asymmetric magnetic coupling structure of UAV wireless charging platform with conformal pickup," *IEEE Trans. Ind. Electron.*, vol. 69, no. 10, pp. 10154–10161, Oct. 2022.

[7] R. Qin, J. Li, J. Sun, and D. Costinett, "Shielding design for high-frequency wireless power transfer system for EV charging with self-resonant coils," *IEEE Trans. Power Electron.*, vol. 38, no. 6, pp. 7900–7909, Jun. 2023.

[8] J. Liu, C. S. Wong, Z. Li, X. Jiang, and K. H. Loo, "An integrated three-phase ac–dc wireless-power-transfer converter with active power factor correction using three transmitter coils," *IEEE Trans. Power Electron.*, vol. 38, no. 6, pp. 7821–7835, Jun. 2023.

[9] Z. Liu, L. Wang, Y. Guo, and S. Li, "Primary-side linear control for constant current/voltage charging of the wireless power transfer system based on the LCC-N compensation topology," *IEEE Trans. Ind. Electron.*, vol. 69, no. 9, pp. 8895–8904, Sep. 2022.

[10] Y. Zhang et al., "A hybrid compensation topology with constant current and constant voltage outputs for wireless charging system," *IEEE Trans. Transp. Electrific.*, vol. 9, no. 2, pp. 2070–2080, Jun. 2023.

[11] G. Buja, M. Bertoluzzo, and K. N. Mude, "Design and experimentation of WPT charger for electric city car," *IEEE Trans. Ind. Electron.*, vol. 62, no. 12, pp. 7436–7447, Dec. 2015.

[12] K. Song et al., "Constant current charging and maximum system efficiency tracking for wireless charging systems employing dual-side control," *IEEE Trans. Ind. Appl.*, vol. 56, no. 1, pp. 622–634, Jan./Feb. 2020.

[13] H.-L. Jou, J.-C. Wu, K.-D. Wu, and C.-Y. Kuo, "Bidirectional dc–dc wireless power transfer based on LCC-C resonant compensation," *IEEE Trans. Power Electron.*, vol. 36, no. 2, pp. 2310–2319, Feb. 2021.

[14] Y. Jiang, L. Wang, Y. Wang, J. Liu, M. Wu, and G. Ning, "Analysis, design, and implementation of WPT system for EV's battery charging based on optimal operation frequency range," *IEEE Trans. Power Electron.*, vol. 34, no. 7, pp. 6890–6905, Jul. 2019.

[15] H. Hu, T. Cai, S. Duan, X. Zhang, J. Niu, and H. Feng, "An optimal variable frequency phase shift control strategy for ZVS operation within wide power range in IPT systems," *IEEE Trans. Power Electron.*, vol. 35, no. 5, pp. 5517–5530, May 2020.

[16] X. Wang, J. Xu, M. Leng, H. Ma, and S. He, "A hybrid control strategy of LCC-S compensated WPT system for wide output voltage and ZVS range with minimized reactive current," *IEEE Trans. Ind. Electron.*, vol. 68, no. 9, pp. 7908–7920, Sep. 2021.

[17] K. Colak, E. Asa, M. Bojarski, D. Czarkowski, and O. C. Onar, "A novel phase-shift control of semibridgeless active rectifier for wireless power transfer," *IEEE Trans. Power Electron.*, vol. 30, no. 11, pp. 6288–6297, Nov. 2015.

[18] Y. Li, J. Hu, F. Chen, Z. Li, Z. He, and R. Mai, "Dual-phase-shift control scheme with current-stress and efficiency optimization for wireless power transfer systems," *IEEE Trans. Circuits Syst. I, Reg. Papers*, vol. 65, no. 9, pp. 3110–3121, Sep. 2018.

[19] R. Mai, Y. Liu, Y. Li, P. Yue, G. Cao, and Z. He, "An active-rectifier-based maximum efficiency tracking method using an additional measurement coil for wireless power transfer," *IEEE Trans. Power Electron.*, vol. 33, no. 1, pp. 716–728, Jan. 2018.

[20] X. Zhang et al., "A control strategy for efficiency optimization and wide ZVS operation range in bidirectional inductive power transfer system," *IEEE Trans. Ind. Electron.*, vol. 66, no. 8, pp. 5958–5969, Aug. 2019.

[21] Y. Jiang, L. Wang, J. Fang, R. Li, R. Han, and Y. Wang, "A high-efficiency ZVS wireless power transfer system for electric vehicle charging with variable angle phase shift control," *IEEE J. Emerg. Sel. Topics Power Electron.*, vol. 9, no. 2, pp. 2356–2372, Apr. 2021.

[22] M. Wu et al., "A dual-sided control strategy based on mode switching for efficiency optimization in wireless power transfer system," *IEEE Trans. Power Electron.*, vol. 36, no. 8, pp. 8835–8848, Aug. 2021.
[23] N. Fu, J. Deng, Z. Wang, W. Wang, and S. Wang, "A hybrid mode control strategy for *LCC–LCC*-compensated WPT system with wide ZVS operation," *IEEE Trans. Power Electron.*, vol. 37, no. 2, pp. 2449–2460, Feb. 2022.
[24] H. Yang et al., "A hybrid load matching method for WPT systems to maintain high efficiency over wide load range," *IEEE Trans. Transp. Electrific.*, vol. 9, no. 1, pp. 1993–2005, Mar. 2023.
[25] S. Chen et al., "An operation mode selection method of dual-side bridge converters for efficiency optimization in inductive power transfer," *IEEE Trans. Power Electron.*, vol. 35, no. 10, pp. 9992–9997, Oct. 2020.
[26] X. Zhu et al., "High-efficiency WPT system for CC/CV charging based on double-half-bridge inverter topology with variable inductors," *IEEE Trans. Power Electron.*, vol. 37, no. 2, pp. 2437–2448, Feb. 2022.
[27] Q. Zhang et al., "Research on input-parallel single-switch wireless power transfer system with constant-current and constant-voltage output," *IEEE Trans. Power Electron.*, vol. 37, no. 4, pp. 4817–4830, Apr. 2022.
[28] Wireless Power Transfer for Light-Duty Plug-In/Electric Vehicles and Alignment Methodology, SAE J2954, 2019.
[29] X. Wang, J. Xu, H. Ma, and S. He, "Inductive power transfer systems with digital switch-controlled capacitor for maximum efficiency point tracking," *IEEE Trans. Power Electron.*, vol. 68, no. 10, pp. 9467–9480, Oct. 2021.
[30] V. Yenil and S. Cetin, "An improved pulse density modulation control for secondary side controlled wireless power transfer system using LCC-S compensation," *IEEE Trans. Ind. Electron.*, vol. 69, no. 12, pp. 12762–12772, Dec. 2022.

Mingyang Li (Graduate Student Member, IEEE) was born in Chongqing, China, in 1997. He received the B.S. degree in vehicle engineering in 2020 from Beijing Institute of Technology, Beijing, China, where he is currently working toward the Ph.D. degree in mechanical engineering.

His research interests include wireless power transfer and phase shift control in dc–dc converters.

Junjun Deng (Member, IEEE) received the B.S., M.S., and Ph.D. degrees in electrical engineering from Northwestern Polytechnical University, Xi'an, China, in 2008, 2011, and 2015, respectively.

From 2011 to 2014, he was a visiting scholar with the Department of Electrical and Computer Engineering, University of Michigan-Dearborn, Dearborn, MI, USA. In 2016, he joined the Faculty of Vehicle Engineering, Beijing Institute of Technology, Beijing, China. His research interests include wireless power transfer, resonant power conversion, and high-performance battery chargers for electric vehicles.

Zhenyuan Zhang (Graduate Student Member, IEEE) was born in Heilongjiang Province, China, in 1999. He received the B.S. degree in vehicle engineering in 2021 from Beijing Institute of Technology, Beijing, China, where he is currently working toward the M.S. degree in mechanical engineering.

His research interests include wireless power transfer and the topology synthesis of dc–dc converters.

Zhenpo Wang (Senior Member, IEEE) received the B.Eng. degree in automotive engineering from Tongji University, Shanghai, China, in 2000, and the Ph.D. degree in automotive engineering from Beijing Institute of Technology, Beijing, China, in 2005.

He is currently a full Professor with the School of Mechanical Engineering, Beijing Institute of Technology, and also the Director of the National Engineering Research Center for Electric Vehicles and the Deputy Head of the Beijing Collaborative Innovation Centre for Electric Vehicles, Beijing, China. In the past five years, he led more than ten national research projects sponsored by the National Natural Science Foundation of China, Ministry of Science and Technology of the People's Republic of China, and Beijing Municipal Science and Technology Committee. He authored or coauthored more than 80 journal papers and 5 monopolies and has been granted 24 invention patents. His research interests include big data technology, battery safety management, wireless charging systems, and advanced vehicle chassis control for electric vehicles.

Dr. Wang is currently the Executive Editor-in-Chief of the *Journal of Green Energy and Intelligent Transportation*. He is also on the Editorial Board of the *China Journal of Highway and Transport*. He was the recipient of several national and municipal science and technology awards.